In Vivo Plasmonic Enhancement of the Photocycle Dynamics and Fluorescence of Genetically Encoded Voltage Indicators

Marco Locarno,[†] Qiangrui Dong,[†] Xin Meng,[†] Cristiano Glessi,[†] Nynke Marije Hettema,[‡] Nidas Brandsma,[†] Sebbe Blokhuizen,[†] Alejandro Castañeda Garcia,[†] Thieme Schmidt,[†] Srividya Ganapathy,[†,¶] Marco Post,[†] Lars van Roemburg,[†] Bing Xu,[§] Chun-Ting Cho,[§] Liedewij Laan,[‡] Miao-Ping Chien,[‖] and Daan Brinks[*,†,‖]

†*Department of Imaging Physics, Delft University of Technology, Delft, The Netherlands*

‡*Department of Bionanoscience, Delft University of Technology, Delft, The Netherlands*

¶*Department of Pediatrics and Cellular and Molecular Medicine, UCSD School of Medicine, San Diego, California, United States*

§*Department of Radiation Science and Technology, Delft University of Technology, Delft, The Netherlands*

‖*Department of Molecular Genetics, Erasmus University Medical Center, Rotterdam, The Netherlands*

* E-mail: d.brinks@tudelft.nl

DOI:

Abstract

The promise of voltage imaging using Genetically Encoded Voltage Indicators (GEVIs) as a neuroscientific technique is hampered by GEVI limitations in brightness, response speed and sensitivity. Biochemical approaches like protein design and evolution are typically used to try and overcome these limitations, but suffer from the large number of possible proteins and mutations in the various GEVI families. Here we approach this problem in a physical way and report that plasmonic coupling to nanoparticles manipulates and enhances the photodynamics and fluorescence of GEVIs in live cells. We designed an optimal nanostar shape for plasmonic coupling through Finite-Difference Time-Domain (FDTD) computational models. We synthesized and characterized the resulting particles and quantified their influence on the brightness, voltage sensitivity, and response speed of the GEVI QuasAr6a. We incorporated the plasmonic enhancement into Markov chain photocycle models of Quasar6a, showing manipulation of both the light-dependent state transitions in the protein and of excited state fluorescence and paving the way for plasmonically enhanced voltage imaging.

Introduction

A comprehensive understanding of electrical signal propagation in neurons holds the potential to advance prevention, diagnosis, and treatment for debilitating disorders of the nervous system.[1–3] Changes in cellular membrane potential can be reported as changes in fluorescence by transmembrane proteins called Genetically Encoded Voltage Indicators (GEVIs).[4] Making movies of neural membrane potential dynamics using this technique is termed Voltage Imaging,[5–7] and enables a choice of better spatial resolution, cellular specificity, response time, and signal fidelity compared to other electrophysiological techniques.[8] Early experiments showed the successful application of GEVIs in Escherichia Coli,[4] Drosophila,[9] and mice[10,11] to investigate the electrical activity of cells and networks in living organisms.

However, GEVIs are not perfect transducers of electrical signals:[12,13] depending on

the GEVI family, they suffer from limitations in response speed and linearity,[9] filtering the electrical signals, or from limitations in fluorescence brightness[14] and voltage sensitivity,[15] limiting their usefulness in noisy in vivo measurements. For example, Archaerhodopsin-based GEVIs, which display a superior sensitivity to voltage in terms of their change in fluorescence brightness,[12] suffer from a quantum yield of approximately 1%[14,16] and are therefore dim in typical neuroscientific imaging experiments.

Typical efforts to create brighter GEVIs focus on biochemical approaches.[17–19] Many efforts have been made to engineer[20–22] or evolve[11,16,23,24] improved GEVIs. Additionally, protein FRET pairs have been used to enhance fluorescence brightness at the expense of voltage sensitivity.[25–27] Here we take a physical approach, inspired by single molecule plasmonic enhancement experiments, where metal nanoparticles are coupled to nearby fluorophores to increase their fluorescence.[28–31]

Plasmonic enhancement can lead to changes in the fluorescence of a dipole in two ways.[28] First, the plasmonic particle can localize an excitation field through resonance or lightning rod effect,[32] leading to the field enhancement $\left|\vec{E}\right|^2 / \left|\vec{E^0}\right|^2$, which in turn leads to more photon absorption per unit time. Second, the probability of a dipole emitting an absorbed photon is given by Fermi's golden rule[29] and can be changed by manipulating the Local Density of Optical States (LDOS) through careful positioning of dielectric or metallic elements in the presence of the dipole.[28,33] This effect is overall quantified by:

$$Y = \frac{\Gamma}{\Gamma + \Gamma_{nr}} \quad , \qquad dY = \frac{\Gamma_{nr}}{(\Gamma + \Gamma_{nr})^2} d\Gamma \tag{1}$$

where Y is the quantum yield of the dipole (i.e. the fraction of absorbed photons that is emitted as photons), Γ is the radiative decay rate and Γ_{nr} is the non-radiative decay rate. In the presence of a standard LDOS, typically defined without the particular manipulation by nanoparticles one has in mind, Y is the characteristic quantum yield of the protein.[28] The presence of a plasmonic particle can manipulate the LDOS and lead to a change in radiative decay rate $d\Gamma$.[28,33] From **Eq. (1)**, it can be seen that this can lead to a significant change in quantum yield dY, provided $\Gamma \ll \Gamma_{nr}$.[30]

We reasoned that judicious design and application of plasmonic particle geometry and spacing might allow us to achieve these effects in vivo, rather than in single-molecule experiments. Moreover, while these effects are typically measured in the manipulation of transitions between ground and electronically excited states of fluorophores,[29,34] we reasoned that in proteins that undergo isomerization and conformational transitions upon absorption and emission of visible or (near)-infrared photons,[18,19] we might be able to influence the protein dynamics as well through plasmonic enhancement. While we found sparse reference to attempts at plasmonic enhancement of fluorescence of proteins,[35–37] one reference attempting fluorescence enhancement of fixed cells labeled with fluorescent dyes,[38] and one in polymer and bacterial environments,[39] we did not find attempts at this in electrophysiologically relevant conditions, let alone while incorporating influence on protein dynamics, and set out to test the feasibility of our idea.

Results and Discussion

Computational modelling

We focused our investigation on the subclass of Archaerhodopsin-based GEVIs (QuasArs[16,24] and Archon[17]) because of their low native quantum yield, and referred to Archon1 as a common template for their structure and function.

Our initial efforts aimed to increase the quantum yield Y of GEVIs. In a first-order approximation, the resonance spectrum of the plasmonic particles should then have maximum overlap with the GEVI emission spectrum, which was measured to be between 640 and 800 nm for Archaerhodopsin-derived sensors.[17,20]

The first question to ask is then which particle geometry and material achieve the best field enhancement. We approached this question through Finite-Difference Time-Domain (FDTD) simulations and investigated a series of nanospheres, nanorods and various types of spiked nanoparticles in biocompatible gold and silver. Gold spheres

exhibited a suboptimal, broad peak in the range of interest (**Fig. S1**), gold nanorods were highly tunable, but the emergence of two resonant modes would have imposed accurate orientation (**Fig. S2**), in the same way as stars with a few sharp tips (**Figs. S3-S4**). On the contrary, highly spiked stars are tunable in the range of interest and are robust to rotation (**Fig. S5**). Gold is a common plasmonic metal characterized by superior biocompatibility and low cytotoxicity;[40] therefore, this material was the elected one throughout the manuscript.

FDTD simulations confirmed that gold nanospheres in water resonate at 520 nm and hence are not suitable for our purpose (**Fig. 1a**), as expected from plasmonic theory.[31] Gold nanostars are however tunable to the optimal wavelength (**Fig. 1a**). Furthermore, the localization of the field around nanospheres spans the entire surface of the sphere and reaches, at best, a field enhancement of the order of tens (**Fig. 1b**). In contrast, the local intensity of the electric fields around the sharp tips of nanostars could be enhanced hundreds- or even thousands-fold (**Fig. 1c**).

Plasmonic enhancement in live biological samples is hampered by the Brownian motion of particles,[41,42] leading to changes in coupling distance and relative orientation between the particle and the emission dipoles and, therefore, noise in the enhancement characteristics. Nanostars might also suffer from irregularities in their makeup, influencing maximum enhancement. Finally, we quantified both effects and found that enhancement by nanostars was robust against the aforementioned noise sources (**Fig 1d,e**, individual simulations available in **Figs. S6-S7**).

Colloidally grown nanostars

To synthesize the gold nanostars, we adapted a colloidal, seed-mediated growth protocol[43] that allowed high shape control and tunability, by optimizing the molar ratio $R = [HAuCl_4]/[seeds]$. We synthesized a series of nanostars under varying seed and growth conditions (**Methods section**). We characterized the synthesized colloids through Energy Dispersive X-ray Spectroscopy (EDX, **Fig. S8**) and Ultraviolet-Visible light (UV-Vis) spectroscopy, and the optimal sample ($R = 30$) was selected based on

the alignment of the absorbance peak to the emission peak of Archon1 (**Fig. 2a**). Although there appeared to be a minor mismatch between the peaks, it could be attributed to a red shift induced by polyvinylpyrrolidone (PVP) as a capping agent (**Eq. (S4)**); once removed, the peaks should align almost perfectly.

Quality control involved immobilizing the gold nanostars onto a silicon substrate via 3-mercaptopropyl trimethoxysilane (MPTMS) (**Fig. 2b**), following a custom protocol (**Methods section**), to examine them under a scanning electron microscope (SEM, **Fig. 2c**). The individual nanostars from the optimal sample exhibited monodispersity and similarity with the simulations, where the average core radius was $r = 23 \pm 5$ nm (mean $\pm$ SD) and the average tip length $l = 12 \pm 3$ nm, (mean $\pm$ SD, **Fig. 2d**). However, the gold nanostars occasionally clustered in micrometre-sized aggregates (**Fig. 2e**), possibly affecting the overall plasmonic resonance and, consequently, the fluorescence enhancement.[44]

Preliminary enhancement tests of Cyanine-5

We next optimized a protocol to localize plasmonic particles to fluorescent dipoles in wet lab conditions. We chose Cyanine-5 (Cy5) as a model molecule to enhance the fluorescence because of its emission peak position and moderate quantum yield ($\sim$30%).[34,45]

We hypothesized that Biotin-Streptavidin binding would provide a suitable way to link nanostars to fluorescent emitters in physiological conditions, and compared the fluorescence signals of Streptavidin-Cy5 (Strep-Cy5), a mixture of Strep-Cy5 and citrate-capped nanostars, and Strep-Cy5 bound to biotin-coated nanostars (**Fig. 3a**) However, we found that the presence of nanostars reduced the fluorescence signal by up to -68 $\pm$ 16% (mean $\pm$ error, propagated from SD, **Fig. 3b**). We attribute this to a combination of the increased optical density in nanostar-containing samples,[46] and fluorescence quenching caused by non-radiative energy transfer from the fluorophore to the nanostar.[47] Streptavidin, the largest molecule in the binding complex, is around 5 nm,[48,49] keeping the fluorophore in the quenching range of the nanostar.[47]

This experiment provided a baseline distance measurement, and we set out to increase the distance between the nanostars and the emitters. Using MPTMS, we immobilized gold nanostars functionalized with a complex of Bovine Serum Albumin (BSA) and biotin on glass, then added Strep-Cy5 (**Fig. 3c**). Fluorescence spectroscopy showed a net 42 ± 6% increase in the fluorescence intensity of Cy5 (peak value ± error, propagated from noise SD, **Fig. 3d**). This value coincides with the estimated value (**Eq. (S7)**) considering the combined lengths of streptavidin (5 nm)[49] and BSA (8 nm)[50] as a spacer larger than the quenching range,[47] the already significant quantum yield of Cy5[34,45] and the estimated average field enhancement of a factor 1.78 from previous simulations (**Fig. S9**).

To use plasmonic enhancement with live cells, the effect needs to be compatible with cell culturing conditions.[51] Our proteins of interest are embedded in the cell membrane, a lipid bilayer.[18] Cells are typically attached to glass substrates using an extracellular matrix protein, like fibronectin.[52] Given the sensitivity of the enhancement to the dielectric environment, we wondered whether the lipid bilayer or fibronectin would influence the enhancement, and whether it would be better to embed nanostars in the fibronectin layer or apply them to the upper surface of cells. To test this, we immobilized nanostars on glass and used Total Internal Reflection Fluorescence (TIRF) microscopy to investigate the effect of an artificial lipid bilayer and a standard fibronectin layer (**Methods section**, **Fig. 3e**). In this in vitro experiment, we positioned lipid bilayers labelled with Cy5 on the sample and imaged the fluorescence with and without nanostars, and with and without fibronectin (**Fig. 3f**). We measured a fluorescence enhancement of 90 ± 50% (mean ± error, propagated from SD) associated with the direct coupling between Cy5 and nanostars, while the presence of the fibronectin layer reduced the effect to 30 ± 50% enhancement (mean ± error, propagated from SD), probably by acting as a spacer (**Fig. 3g**).[47] In combination with the Strep-Cy5 results (**Fig. 3d**), we estimate the distance between the Cy5 molecules and the nanostars to be 14.5 nm, respectively 8.5 nm with and without fibronectin (**Fig. 3h**), providing an estimate for the thickness of the fibronectin layer amounting to 6 nm.

Plasmonic enhancement of QuasAr fluorescence in live cells

Having shown that cell membrane embedding and fibronectin application do not hinder plasmonic enhancement of fluorophores, we performed a simple addition of colloidal nanostars to HEK293T cells expressing either QuasAr1 (**Fig. 4a**) or QuasAr6a (**Fig. 4b**).

We noticed an enhancement in the fluorescence of individual cells over time (**Fig. 4c**). We quantified the time course of cell population fluorescence after the addition of the nanostars and noticed an increase of fluorescence to a factor 140 ± 80% (QuasAr1, mean ± error, propagated from SE, **Fig 4a**) and 28 ± 12% (QuasAr6a, mean ± error, propagated from the SE, **Fig 4b**) respectively.

We tested the difference between simple application of nanostars and embedding them in the fibronectin layer. We immobilized gold nanostars on glass, coated the surface with fibronectin, and plated HEK293T cells expressing QuasAr6a (**Fig. 4d**). We performed a population screen of fluorescence at the bottom surface of the cells (**Fig 4e**) and achieved a fluorescence enhancement of 69 ± 19% (median ± error, propagated from the SE), confirmed by the fluorescence brightness of the median cell in a control, respectively enhanced sample (**Fig. 4f**). The difference in enhancement of fluorescence between the nanostars applied to the top surface, respectively embedded in the fibronectin adhesion layer, indicates that the glycocalyx[53–55] surrounding the cells acts as an effective spacer between the fluorophores and the nanoparticles applied to the top surface of the cells.

Photocycle manipulation via plasmonic enhancement

Fluorescence enhancement of dim voltage sensors is one possible application of combining GEVIs with nanostars. Given that the kinetics of GEVIs are determined by a photocycle with absorption and potential emission events at multiple stages,[18,56–60] we hypothesized that interaction with plasmonic particles might also impact voltage sensitivity and response speed. We performed a voltage clamp experiment on HEK293T

cells expressing QuasAr6a plated on fibronectin over immobilized gold nanostars to test this. We varied the voltage across the cell membrane in steps from -70 to +30 mV and recorded the fluorescence response without (**Fig. 5a**) and with (**Fig. 5b**) nanostars in the fibronectin layer. We noticed a decrease in voltage sensitivity from a DF/F of 0.38 ± 0.07 to 0.11 ± 0.04 (mean ± SD, **Fig. 5c**) and an increase in response speed from $\tau_{up} = 7 \pm 2$ ms to $\tau'_{up} = 0.8 \pm 0.1$ ms and $\tau_{down} = 6 \pm 2$ ms to $\tau'_{down} = 1.1 \pm 0.5$ ms (mean ± SD, **Fig. 5d**). The measured time constant of the plasmonically enhanced response was limited by the camera response time, rather than the protein kinetics.

Following the template photocycle for Arch,[57] we modeled a phenomenological photocycle for QuasAr6a as a continuous-time finite-state Markov chain (**Fig. 5e**).[61] Here, the M→N transition is voltage sensitive, the N→Q transition is photoactivatable, and Q is the excitable fluorescent state. We modelled fluorescence as proportional to Q-state population multiplied by field enhancement and fitted our data to models with varying transition rates and field enhancement. We found the best fit to the data, including enhanced brightness, decreased voltage sensitivity and faster kinetics, for a model incorporating $k_3 = 24$ s^{-1} without plasmonic enhancement and $k_3 = 1131$ s^{-1} and $\left|\vec{E}\right|^2 / \left|\vec{E}^0\right|^2 = 0.15$ with plasmonic coupling (**Fig. 5f**, complete parameters and results available in **Tables S1-S2**). Enhancement of only the quantum yield evidently does not explain the change in kinetics (**Fig. S10a**), and enhancement of only k_3 leads to a worse fit of the data (**Fig. S10b**). We interpreted the enhancement of k_3 and the reduced decay rate enhancement both as consequences of suboptimal coupling distance, resulting on one hand in the quenching of the fluorescence, and on the other in a strong localized field that affects the photoactivatable transition.

Discussion

This study shows the potential for enhancing both fluorescence and photosensitive protein kinetics using plasmonic enhancement in vivo. The emergence of noticeable

fluorescence enhancement, even without precise control over the coupling distance, suggested a robust effect that could be applied in vivo. Moreover, because plasmonic enhancement is a fast physical phenomenon lasting tens of femtoseconds,[62] it would be compatible with multiphoton excitation or other nonlinear imaging methods. In this study, we showed the influence of the glycocalyx on the measured enhancement. The glycocalyx can be used as a natural spacer layer, and its influence can be tuned by the binding protocol used to link nanoparticles to membrane proteins. This approach also opens up the possibility of enhancing the absorption and signal transduction of naturally occurring opsins and GPCRs. Interestingly, the photocycle simulations seemed to indicate that the glycocalyx does not contribute to the distance control when fluorescent cells are plated on a layer of fibronectin embedding the nanostars, keeping the fluorophore at the edge of the quenching regime. This is because fibronectin binds directly to integrins present in the cell membrane,[63] minimizing the coupling distance to the fibronectin thickness. We hypothesize that a controlled trade-off between the enhancement of absorption (k_3) and emission (Y) can be used to fine-tine voltage sensitivity, speed, and brightness of GEVIs. Protein evolution of GEVIs often leads to increases in brightness at the expense of decreases in the speed of response to voltage changes.[19] Plasmonic enhancement shows a way to achieve both effects simultaneously.

Conclusions

We showed the design and creation of gold nanostars for the enhancement of fluorescence and protein kinetics of QuasAr-based GEVIs. We investigated the effect of electrophysiologically realistic dielectric environments on this effect and showed increases in response speed to voltage and fluorescence brightness.

Methods

FDTD simulations

Finite-difference time-domain (FDTD) numerical simulations were conducted using Lumerical's FDTD Solutions, with scripts available on GitHub.[64] Simulations of gold nanospheres involved varying the radius R of a gold sphere submerged in water, with a focus on assessing the maximum field enhancement $|E|^2/|E^0|^2$ within a small cubic volume ($\Delta x = \Delta y = \Delta z = R/2$) located 4 nm from the surface. Simulations covered a range of radii ($R_{\text{min}} = 6$ nm to $R_{\text{max}} = 76$ nm) with 2 nm steps.

Gold nanostar models were crafted based on SEM micrographs of synthesized nanoparticles. To generate these models, Blender software was employed to create complex meshes. The starting point for this modelling was an icosahedron shape, with its vertices extended to mimic the tip arrangement found on real nanostars. To ensure smoother surfaces, a Subdivision Surface Modifier was applied. During these simulations, a mesh size of 35 Meshes Per Radius (MPR) was consistently used. For benchmarking, a model nanostar with a core radius R of 25 nm and a tip length L_{tip} of 10 nm was adopted. For the simulations shown in **Figs. 1d** and **1e**, a core radius of 30 nm was used. Simulations explored variations in tip density and randomness to understand their implications for field enhancement. These variations included the random omission of tips and the random displacement of tip vertices, quantified using a "randomness factor" in Blender ranging from 0 to 1. Since the sharp tips simulated in **Figs. 1a**, **1c**, and **1d** generated unphysical fields when randomized in Blender, we introduced an adaptation to their sharpness to prevent unrealistic stretching and overly sharp edges. All scripts for Lumerical and Blender can be found on GitHub.[64]

Colloidal synthesis

In the presence of a high concentration of polyvinylpyrrolidone (PVP) dissolved in dimethylformamide (DMF), highly branched nanostars can be obtained efficiently at room temperature.[65] Briefly, gold tips can grow on pre-formed gold seeds thanks to the reducing power of DMF and the excess of PVP. The protocol for making PVP-coated gold nanostars is based on the seed-mediated synthesis proposed by Barbosa et al.,[43] where gold spherical seeds of 15 nm of radius have been employed, and the last purification step has been carried out twice to minimize the cytotoxic effect of DMF. Given the estimated concentration of the gold seed solution (0.5 mM), 273 μL of seeds were added to 15 mL of 10 mM PVP (Sigma-Aldrich, PVP10) dissolved in DMF (Sigma-Aldrich, D4551), guaranteeing a controlled molar ratio of 30.

UV/Visible spectroscopy of gold nanostars colloid

The absorbance spectra were measured using a compact Visible-NIR light source (ecoVIS by Ocean Optics) together with a compact STS spectrometer (STS-VIS Microspectrometer, 350 – 800 nm, by Ocean Insight). Absorbance was measured using an integration time of 5.1 ms after background subtraction and intensity calibration, and averaged 1000 times.

MPTMS surface coating and nanoparticle immobilization

For the preparation of the MPTMS-coated dishes, a 10% MPTMS solution was prepared as follows: MPTMS (2.50 mL, Sigma-Aldrich, 175617) was combined with MilliQ water (2.50 mL), acetic acid (1.67 mL, Sigma-Aldrich, ARK2183), and pure ethanol (18.3 mL, Sigma-Aldrich, EMSURE 1.00983.1000). Prior to use, glass bottom dishes (Cellvis, D35-14-1.5-N) and fragments of silicon wafers were cleaned using oxygen plasma for 1 to 2 minutes, and all subsequent reactions were completed within a 30-minute timeframe. To prepare the substrates for cellular imaging, approximately 150 μL of the MPTMS solution was gently dispensed into the recessed wells of the imaging dishes. These dishes were then carefully transferred to a large glass beaker and purged with nitrogen for 30 minutes (or until dry). Any residual MPTMS was aspirated. The dishes were subsequently subjected to a series of rinsing steps, including one wash with 150 μL of pure ethanol in the recessed well, one wash with 2 mL of pure ethanol across the entire dish, and a final rinse with 2 mL of MilliQ water across the entire dish. To ensure dryness, the dishes were placed in a vacuum oven at 65°C for 2 hours. 200 μL of gold nanostars were uniformly added to cover each recessed well. The dishes were then incubated overnight in a 37°C incubator, ensuring their cleanliness and contamination-free environment. Subsequently, the nanostar-coated substrates were aspirated, subjected to two 2 mL MilliQ water washes, and dried to near dryness. They were stored in the incubator until their intended use. For silicon substrates, the protocol remained unchanged, with volumes adjusted proportionally to the chip's surface area.

SEM/EDX characterization

SEM imaging was performed in a Thermo Fisher Scientific (TFS) Nova 600i Nano Lab dual-beam system with a primary beam energy of 5 kV and nominal current of 0.27 nA using the SE-TLD detector. All imaging was performed at 5mm working distance and in immersion mode. Horizontal field of view and dwell time were varied and are specified on each reported image. EDX measurements were performed in the same Nova Nanolab dual-beam SEM using an Oxford Instruments X-MAX 80 EDX detector. The working distance was kept at 5 mm to have the optimum EDX signal. Spectra were analyzed using the Oxford Instruments AZtec software. The reported map EDX was obtained with a primary beam energy of 5 kV. Si and O are mapped and reported in weight percentage (Wt%).

SEM image analysis

We aimed to isolate individual nanoparticles in SEM images to characterize them based on their core radius and tip length. Therefore, an algorithm was created using Python and OpenCV, available on GitHub.[64] Firstly, the algorithm segmented the nanoparticles from the background using an Otsu adaptative threshold for bi-multimodal histograms. Secondly, an erosion was executed on the binary mask with 5 iterations and a 3×3 kernel to separate close nanoparticles. This way, we isolated the center of mass of the nanoparticles to iterate over the individual contours and generate individual masks for each nanoparticle; on the individual mask, we performed a symmetric dilatation to revert the previous erosion. Next, from the mask of the individual nanoparticles, we calculated the inner maximum radius to find the core size and the minimum enclosing circle

to get the total radius and the tip length. Finally, we extracted the pixel/meters conversion factor using the images' metadata for further analysis.

Aggregates that were still detected as single nanoparticles have been filtered post-analysis by applying the 2σ criterion on both radius and tip length.

Fluorescence assays in solution

Experiments in **Figs. 2**, **3.f**, **3.g**, **4** and **5** were performed with nanostars grown in-house; experiments in **Figs. 3.b** and **3.d** were performed with commercially available nanostars.

Commercial gold nanostars (100 nm) as well as biotin-functionalized gold nanostars (100 nm), were obtained from Cytodiagnostics (Catalog number: GU-100-100). Notably, their absorption maxima are closely aligned with our in-house synthesized nanostars. The experiments were conducted using standard 96-well plates. 10 nM nanostars or biotin-functionalized nanostars, Streptavidin-Cy5 (10 μM, ThermoFisher Scientific) were introduced into the respective sample groups. Each group was prepared with three replicates to ensure statistical robustness.

The 96-well plates, housing the nanostars and Streptavidin-Cy5 samples, were incubated at 37 °C for one hour to ensure complete binding between the components. Following this incubation, the fluorescence emissions were quantified and recorded with a Cary Eclipse Fluorescence Spectrophotometer (Agilent Technologies).

Fluorescence spectroscopy assays on substrates

Glass coverslips underwent the MPTMS surface coating and nanoparticle immobilization, as indicated above. Approximately 60 μL of this MPTMS solution was applied to the glass coverslips. The uniform layer of gold nanostars (AuNS) was deposited onto the substrates by adding 1 mL of AuNS solution to each recessed well.

The containers housing the glass slides were then sealed and placed on an orbital shaker (100 rpm) in a dark environment for an incubation period of 18 hours. On the following day, the AuNS-coated glass slides underwent three meticulous rinses with Milli-Q water, followed by gentle drying under a stream of nitrogen gas. To form monolayers of biotinylated bovine serum albumin (bBSA) on the substrates, 200 μL of a 100 μg/mL bBSA solution in PBS was applied to the substrate surfaces and allowed to incubate for 1 hour in a 37℃ incubator. 40 μL of a 10 μM Streptavidin-Cy5 solution was added to the substrate surfaces and incubated for 2 hours in a 37 ℃ incubator. Following the incubation, the substrates were rinsed 3 times with PBS to eliminate any unbound fluorophores and gently dried using a nitrogen gas stream.

Fluorescence emission spectra of Streptavidin-Cy5 were measured using a photomultiplier tube (R7600U-20, Hamamatsu) coupled to a monochromator (SP2300, Princeton Instruments). Excitation light was provided by a xenon lamp connected to a monochromator (Gemini 180, HORIBA).

Supported lipid bilayer formation

A glass slide covered by a silicone gasket with four 100 μl wells was prepared with different MPTMS-immobilized nanostars and fibronectin conditions prior to the bilayer formation. The two Avanti Polar lipids (Birmingham,

AL) used were 1,2-dioleoyl-sn-glycero-3-phosphocholine (DOPC) and 1,2-dioleoyl-sn-glycero-3-phosphocholine-N-(Cyanine 5) (DOPC-Cy5). Lipids in chloroform were mixed in a molar ratio of 99.5:0.5 DOPC:DOPC-Cy5 in a glass vial. The chloroform was evaporated with nitrogen and dried in a vacuum desiccator overnight. The dried lipid film was resuspended in PBS. The glass vial with the solution was then vortexed in bursts of 30 seconds with 1-minute intervals to resuspend all lipids and to stimulate the self-assembly of multilamellar vesicles. The solution was then sonicated in a high-capacity bath sonicator (10% amplitude, 10 s on, 10 s off, for one hour) to get a uniform size distribution of liposomes. 100 μl of liposome solution was then deposited in each of the wells of the silicone gasket. The glass slides with liposomes were incubated for 30 min at room temperature to allow for supported lipid bilayer formation. All wells were washed four times with 200ul PBS after incubation.

TIRF microscopy

For the TIRF microscopy, an inverted microscope (NikonTi2-E, motorized) equipped with a 100× oil immersion objective (Nikon Apo TIRF 1.49 NA) and an Andor iXon Ultra 897 camera was used. The microscope was upgraded with an azimuthal TIRF/FRAP illumination module (GATACA systems iLAS 2). Samples were exited at 642 nm at 10% laser power(GATACA CW laser, 642nm/110mW). The emission was filtered with a 706/90 filter. Samples were exited for 200 ms for each frame, and a multiplication gain 50 was used. The penetration depth automatically estimated by the system is 106 nm.

HEK293T culture

HEK293T cells (Catalog number ATCC® CRL-3216™) with passage number ¡30 were cultured in Dulbecco's Modified Eagle Medium (DMEM) supplemented with 10% Fetal Bovine Serum (VWR Seradigm Premium Grade), 50 units/mL Penicillin (Life Technologies), 50 μg/mL Streptomycin (Life Technologies), and 1% GlutaMAX (Life Technologies) at 37 °C under 10% CO_2.

Lentivirus preparation and transduction

For lentivirus production, HEK293T cells were seeded at $4{\cdot}10^6$ cells per 100 mm polystyrene dish (Sarstedt) 1 day before transfection in order to achieve 80% confluency at the moment of transfection. Cells were co-transfected with 1.5 μg transfer plasmid carrying either QuasAr1 or QuasAr6a, 5 μg of pMDLg/RRE (Addgene plasmid #12251), 5 μg of pRSV/Rev (Addgene plasmid #12253), and 3.5 μg of pMD2.G (Addgene plasmid #12259) mixed in 400 μL pre-warmed opti-MEM with 60 μL polyethylenimine solution (1 μg/μL in PBS). 8 hours post-transfection, medium was replaced with fresh cell culture medium including 25 mM HEPES. Lentivirus-containing supernatant was collected 48 and 72 hours post-transfection. Supernatant collected 48 hours post-transfection was stored overnight at 4 °C before pooling it with lentivirus collected 72 hours post-transfection. Supernatant was filtered through 0.22 μm PVDF filters. Lentivirus was concentrated 15-fold using LentiX concentrator reagent (Takara), resuspended in PBS, and stored at -80 °C in 100 μL aliquots. μ

For lentiviral transduction, $2.5 \cdot 10^5$ cells were seeded per 35 mm polystyrene dish (Sarstedt) 1 day before transduction in order to achieve 50% confluency at the moment of transduction. Lentiviral aliquots were rapidly thawed in a 37 °C water bath. 100 μL of concentrated virus was added per dish. Cells were incubated with lentivirus for 24 hours, after which the media was replaced with fresh cell culture medium.

Widefield fluorescence microscopy

A custom-built[66] widefield microscope was employed to investigate the fluorescence of the QuasArs expressed in cells. Two continuous wave laser sources (MLL-FN-639 CNI and OBIS 488 LX, by Coherent) were made uniform in polarization and beam diameter through zero-order half-wave plates (WPH05M-488 and WPH05M-633 by Thorlabs), polarizers (CCM5-PBS201/M by Thorlabs) and individual collimators (AC254 mounted achromatic doublets by Thorlabs). The beams were then combined using a dichroic mirror (DMLP505 by Thorlabs) and led through an acousto-optic tunable filter (AOTFnC-VI S by AA Optoelectronics) with a modulation rate of 22 kHz. With the exception of the patch clamp voltage imaging experiments, the beam diameter was expanded with a telescope (AC254 mounted achromatic doublets by Thorlabs) using flip mounts (TRF90/M by Thorlabs). The light was reflected from a Digital Micromirror Device (DMD, Vialux V7001 by Texas Instruments) into a tube lens (TTL200 by Thorlabs) and projected by the objective (Olympus XLPLN25XWMP2, NA 1.05, working distance 2 mm) onto the sample. The emitted fluorescence was reflected by a dichroic mirror (Di03-R405/488/532/635-t3-32 × 44 by Semrock), collected using a tube lens (TTL200 by Thorlabs) and filtered further depending on the emission range (FF01560/94-25, FF01-582/64-25, LP02-664RU-25 and FF01-790/SP-25 by Semrock), before reaching the sCMOS camera (ORCA Flash4.0 V3, 2048 × 2048 pixels, 6.5 μm pixel size by Hamamatsu) where the image was captured in a low-noise configuration with a total magnification of 27.8.

The maximum powers after the objective in the telescope configuration are 40 mW for the 639 nm laser and 2 mW for the 488 nm laser; without the telescope, the powers are 122 mW for the 639 nm laser and 5.2 mW for the 488 nm laser.

Whole-cell patch-clamp recordings

Patch-clamp technique and imaging was performed 72 hours after lentiviral transduction. Transduced cells were seeded in the 14mm glass well of fibronectin-coated glass bottom dishes (Cellvis) at a density of $1.5 \cdot 10^4$ cells per well 24 hours before the patch-clamp experiment. Before patch-clamp procedure, cells were washed gently three times with 2 mL of pre-warmed extracellular buffer (EC buffer). Cells were immersed in 2 mL of EC buffer throughout the patch clamp procedure. Constitution of EC buffer is 125 mM NaCl, 2.5 mM KCl, 3 mM CaCl2, 1 mM MgCl2, 15 mM HEPES, and 30 mM glucose.[67] pH of EC buffer is adjusted to 7.3 with NaOH. Osmolarity of EC buffer is adjusted to 300 mOsm with sucrose.

Borosilicate glass micropipettes were pulled from capillaries (Sutter Instrument) and filled with 10 μL of intracellular medium (IC medium). Constitution of IC medium is 125 mM K-gluconate, 8 mM NaCl, 0.6 mM MgCl2, 0.1 mM CaCl2, 1 mM EGTA, 10 mM HEPES, 4 mM Mg-ATP and 0.4 mM Na-GTP, with pH adjusted to 7.3 with KOH.[68] Osmolarity of IC medium is adjusted to 295 mOsm with sucrose. Tip resistance was verified to be between 5 and 10 MΩ. Cellular responses were evoked through voltage steps ranging from -70 mV to

+30 mV at a frequency of 5 Hz, while the fluorescence of QuasAr1 and QuasAr6a was excited at 639 nm. The camera frame rate in this setting is 1000 fps.

Photocycle modelling and simulation

The photocycle of QuasAr6a has been modelled as a 4-state continuous-time Markov chain, where the putative biological macrostates corresponded directly to the mathematical states. Transitions were considered unidirectional. The Markov chain was expressed as a system of linear ODEs and solved numerically in Python using the LSODA solver (Livermore Solver for Ordinary Differential equations with Automatic method switching for stiff and non-stiff problems). The features of simulated traces (brightness enhancement, voltage sensitivities, response speeds) are compared to those of the measured traces and improved following a custom-made genetic algorithm, where new parameters are randomly affected by Gaussian noise with predefined characteristics. After every 2000 generations, the best parameters are picked for the successive round of random variations. After repeating this process 50 times (for a total of 10000 generations), the software outputs the best parameters, unless a plateau is reached before. To quantify the goodness of the fit in different conditions, we employed the χ^2 metrics on the fitted features compared to the one from the simulations. A lower χ^2 indicates a better agreement of the simulations with the data. The fitted values for the models can be consulted in the Supplementary Information, while the code can be accessed on GitHub.[64]

Authors' contributions

Table 1: Authors' contributions according to CRediT taxonomy.

Task	**ML**	**QD**	**XM**	**CG**	**NMH**	**NB**	**SB**	**ACG**	**TS**	**SG**	**MP**	**LR**	**BX**	**CTC**	**LL**	**MPC**	**DB**
Conceptualization	■	■		▒					■								■
Methodology	■	■	■		▒	▒		▒	▒	▒						▒	■
Formal analysis	■					▒	▒	▒									
Software	■		■			■	■	■									■
Investigation	■	■	▒	■	■	▒	▒		▒		▒	▒	▒	▒			
Validation	■	■	▒	▒	▒	▒	▒		▒		▒	▒	▒	▒			■
Resources	■	■	■	■	▒				▒	■	■		▒	▒	■	▒	■
Data Curation	■	■	▒	▒	▒	▒	▒	▒	▒								■
Visualization	■																
Writing (Original Draft)	■	▒		▒	▒			▒									■
Writing (Review & Editing)	■	▒	▒	▒	▒	▒	▒	▒	▒	▒	▒	▒	▒	▒	▒	▒	■
Project administration																	■
Supervision															■	■	■
Funding acquisition	▒	■															■

Acknowledgments

We thank Ryan Lane for preliminary SEM images that did not make it to the final draft, Zimu Wei for UV-Visible spectroscopy measurements that did not make it to the final draft, Zhenzhen Wu for lifetime experiments that did not make it to the final draft, Ornella Cavalleri and Claudio Canale for suggesting the use of MPTMS, Antonia Denkova and Erik van der Kolk for training and use of facilities. ML acknowledges support from the Erasmus+ Traineeship programme. QD acknowledges support from the Chinese Scholarship Council scholarship. DB acknowledges support from an NWO Start-up Grant (740.018.018) and ERC Starting Grant (850818 - MULTI-VIsion), as well as an NWO XS grant (OCENW.XS2.033), and by the Delft AI initiative (Ailab BIOlab) and the Convergence Health and Technology (Integrative Neuromedicine flagship).

References

(1) Hausser, M.; Spruston, N.; Stuart, G. J. Diversity and dynamics of dendritic signaling. *Science* **2000**, *290*, DOI: 10.1126/science.290.5492.739.

(2) Vetter, P.; Roth, A.; Häusser, M. Propagation of action potentials in dendrites depends on dendritic morphology. *Journal of Neurophysiology* **2001**, *85*, DOI: 10.1152/jn.2001.85.2.926.

(3) Feigin, V. L.; Vos, T.; Nichols, E.; Owolabi, M. O.; Carroll, W. M.; Dichgans, M.; Deuschl, G.; Parmar, P.; Brainin, M.; Murray, C. The global burden of neurological disorders: translating evidence into policy. *The Lancet Neurology* **2020**, *19*, DOI: 10.1016/S1474-4422(19)30411-9.

(4) Kralj, J. M.; Hochbaum, D. R.; Douglass, A. D.; Cohen, A. E. Electrical spiking in Escherichia coli probed with a fluorescent voltage-indicating protein. *Science* **2011**, *333*, DOI: 10.1126/science.1204763.

(5) Carter, M.; Shieh, J. C. *Guide to Research Techniques in Neuroscience*; 2010; DOI: 10.1016/C2009-0-01891-1.

(6) Gasparini, S.; Palmer, L. M. Dendrites: Recording from fine neuronal structures using patch-clamp and imaging techniques. *Neuromethods* **2016**, *113*, 97–121, DOI: 10.1007/978-1-4939-3411-9.

(7) Peterka, D. S.; Takahashi, H.; Yuste, R. Imaging Voltage in Neurons. *Neuron* **2011**, *69*, DOI: 10.1016/j.neuron.2010.12.010.

(8) Yang, H. H.; St-Pierre, F. Genetically encoded voltage indicators: Opportunities and challenges. *Journal of Neuroscience* **2016**, *36*, DOI: 10.1523/JNEUROSCI.1095-16.2016.

(9) Cao, G.; Platisa, J.; Pieribone, V. A.; Raccuglia, D.; Kunst, M.; Nitabach, M. N. Genetically targeted optical electrophysiology in intact neural circuits. *Cell* **2013**, *154*, DOI: 10.1016/j.cell.2013.07.027.

(10) Knöpfel, T.; Gallero-Salas, Y.; Song, C. Genetically encoded voltage indicators for large scale cortical imaging come of age. *Current Opinion in Chemical Biology* **2015**, *27*, DOI: 10.1016/j.cbpa.2015.06.006.

(11) Adam, Y. et al. Voltage imaging and optogenetics reveal behaviour-dependent changes in hippocampal dynamics. *Nature* **2019**, *569*, DOI: 10.1038/s41586-019-1166-7.

(12) Storace, D.; Sepehri Rad, M.; Kang, B. E.; Cohen, L. B.; Hughes, T.; Baker, B. J. Toward Better Genetically Encoded Sensors of Membrane Potential. *Trends in Neurosciences* **2016**, *39*, DOI: 10.1016/j.tins.2016.02.005.

(13) Bando, Y.; Sakamoto, M.; Kim, S.; Ayzenshtat, I.; Yuste, R. Comparative Evaluation of Genetically Encoded Voltage Indicators. *Cell Reports* **2019**, *26*, DOI: 10.1016/j.celrep.2018.12.088.

(14) Flytzanis, N. C.; Bedbrook, C. N.; Chiu, H.; Engqvist, M. K.; Xiao, C.; Chan, K. Y.; Sternberg, P. W.; Arnold, F. H.; Gradinaru, V. Archaerhodopsin variants with enhanced voltage-sensitive fluorescence in mammalian and Caenorhabditis elegans neurons. *Nature Communications* **2014**, *5*, DOI: 10.1038/ncomms5894.

(15) Sung, U.; Sepehri-Rad, M.; Piao, H. H.; Jin, L.; Hughes, T.; Cohen, L. B.; Baker, B. J. Developing fast fluorescent protein voltage sensors by optimizing FRET interactions. *PLoS ONE* **2015**, *10*, DOI: 10.1371/journal.pone.0141585.

(16) Hochbaum, D. R. et al. All-optical electrophysiology in mammalian neurons using engineered microbial rhodopsins. *Nature Methods* **2014**, *11*, DOI: 10.1038/NMETH.3000.

(17) Silapetere, A. et al. QuasAr Odyssey: the origin of fluorescence and its voltage

sensitivity in microbial rhodopsins. *Nature Communications* **2022**, *13*, 5501, DOI: 10.1038/s41467-022-33084-4.

(18) de Grip, W. J.; Ganapathy, S. Rhodopsins: An Excitingly Versatile Protein Species for Research, Development and Creative Engineering. *Frontiers in Chemistry* **2022**, *10*, DOI: 10.3389/fchem.2022.879609.

(19) Meng, X.; Ganapathy, S.; van Roemburg, L.; Post, M.; Brinks, D. Voltage Imaging with Engineered Proton-Pumping Rhodopsins: Insights from the Proton Transfer Pathway. *ACS Physical Chemistry Au* **2023**, *3*, DOI: 10.1021/acsphyschemau.3c00003.

(20) Kralj, J. M.; Douglass, A. D.; Hochbaum, D. R.; MacLaurin, D.; Cohen, A. E. Optical recording of action potentials in mammalian neurons using a microbial rhodopsin. *Nature Methods* **2012**, *9*, DOI: 10.1038/nmeth.1782.

(21) Jin, L.; Han, Z.; Platisa, J.; Wooltorton, J. R.; Cohen, L. B.; Pieribone, V. A. Single Action Potentials and Subthreshold Electrical Events Imaged in Neurons with a Fluorescent Protein Voltage Probe. *Neuron* **2012**, *75*, DOI: 10.1016/j.neuron.2012.06.040.

(22) St-Pierre, F.; Marshall, J. D.; Yang, Y.; Gong, Y.; Schnitzer, M. J.; Lin, M. Z. High-fidelity optical reporting of neuronal electrical activity with an ultrafast fluorescent voltage sensor. *Nature Neuroscience* **2014**, *17*, DOI: 10.1038/nn.3709.

(23) Piatkevich, K. D. et al. A robotic multidimensional directed evolution approach applied to fluorescent voltage reporters article. *Nature Chemical Biology* **2018**, *14*, DOI: 10.1038/s41589-018-0004-9.

(24) Tian, H. et al. Video-based pooled screening yields improved far-red genetically encoded voltage indicators. *Nature Methods* **2023**, DOI: 10.1038/s41592-022-01743-5.

(25) Zou, P.; Zhao, Y.; Douglass, A. D.; Hochbaum, D. R.; Brinks, D.; Werley, C. A.; Harrison, D. J.; Campbell, R. E.; Cohen, A. E. Bright and fast multicoloured voltage reporters via electrochromic FRET. *Nature Communications* **2014**, *5*, DOI: 10.1038/ncomms5625.

(26) Abdelfattah, A. S.; Farhi, S. L.; Zhao, Y.; Brinks, D.; Zou, P.; Ruangkittisakul, A.; Platisa, J.; Pieribone, V. A.; Ballanyi, K.; Cohen, A. E.; Campbell, R. E. A bright and fast red fluorescent protein voltage indicator that reports neuronal activity in organotypic brain slices. *Journal of Neuroscience* **2016**, *36*, DOI: 10.1523/JNEUROSCI.3484-15.2016.

(27) Abdelfattah, A. S. et al. Bright and photostable chemigenetic indicators for extended in vivo voltage imaging. *Science* **2019**, *365*, DOI: 10.1126/science.aav6416.

(28) Geddes, C. D.; Lakowicz, J. R. Metal-Enhanced Fluorescence. Journal of Fluorescence. 2002; DOI: 10.1023/A:1016875709579.

(29) Kühn, S.; Håkanson, U.; Rogobete, L.; Sandoghdar, V. Enhancement of single-molecule fluorescence using a gold nanoparticle as an optical nanoantenna. *Physical Review Letters* **2006**, *97*, DOI: 10.1103/PhysRevLett.97.017402.

(30) Amendola, V.; Pilot, R.; Frasconi, M.; Maragò, O. M.; Iatì, M. A. Surface plasmon resonance in gold nanoparticles: A review. *Journal of Physics Condensed Matter* **2017**, *29*, DOI: 10.1088/1361-648X/aa60f3.

(31) Locarno, M.; Brinks, D. Analytical calculation of plasmonic resonances in metal nanoparticles: A simple guide. *American Journal of Physics* **2023**, *91*, 538, DOI: 10.1119/5.0094967.

(32) Fukuoka, N.; Tanabe, K. Lightning-rod effect of plasmonic field enhancement on hydrogen-absorbing transition metals. *Nanomaterials* **2019**, *9*, DOI: 10.3390/nano9091235.

(33) Li, J. F.; Li, C. Y.; Aroca, R. F. Plasmon-enhanced fluorescence spectroscopy. *Chemical Society Reviews* **2017**, *46*, DOI: 10.1039/c7cs00169j.

(34) Fu, Y.; Zhang, J.; Lakowicz, J. R. Plasmonic enhancement of single-molecule fluorescence near a silver nanoparticle. *Journal of Fluorescence* **2007**, *17*, DOI: 10.1007/s10895-007-0259-0.

(35) Donehue, J. E.; Wertz, E.; Talicska, C. N.; Biteen, J. S. Plasmon-Enhanced brightness and photostability from single fluorescent proteins coupled to gold nanorods. *Journal of Physical Chemistry C* **2014**, *118*, DOI: 10.1021/jp504186n.

(36) Fu, B.; Flynn, J. D.; Isaacoff, B. P.; Rowland, D. J.; Biteen, J. S. Super-Resolving the Distance-Dependent Plasmon-Enhanced Fluorescence of Single Dye and Fluorescent Protein Molecules. *Journal of Physical Chemistry C* **2015**, *119*, DOI: 10.1021/acs.jpcc.5b05154.

(37) Barulin, A.; Claude, J. B.; Patra, S.; Bonod, N.; Wenger, J. Deep Ultraviolet Plasmonic Enhancement of Single Protein Autofluorescence in Zero-Mode Waveguides. *Nano Letters* **2019**, *19*, DOI: 10.1021/acs.nanolett.9b03137.

(38) Theodorou, I. G.; Ruenraroengsak, P.; Gonzalez-Carter, D. A.; Jiang, Q.; Yagüe, E.; Aboagye, E. O.; Coombes, R. C.; Porter, A. E.; Ryan, M. P.; Xie, F. Towards multiplexed near-infrared cellular imaging using gold nanostar arrays with tunable fluorescence enhancement. *Nanoscale* **2019**, *11*, DOI: 10.1039/c8nr09409h.

(39) Lee, S. A.; Biteen, J. S. Interplay of Nanoparticle Resonance Frequency and Array Surface Coverage in Live-Cell Plasmon-Enhanced Single-Molecule Imaging. *Journal of Physical Chemistry C* **2018**, *122*, DOI: 10.1021/acs.jpcc.8b01436.

(40) Shukla, R.; Bansal, V.; Chaudhary, M.; Basu, A.; Bhonde, R. R.; Sastry, M. Biocompatibility of gold nanoparticles and their endocytotic fate inside the

cellular compartment: A microscopic overview. *Langmuir* **2005**, *21*, DOI: 10.1021/la0513712.

(41) Uhlenbeck, G. E.; Ornstein, L. S. On the theory of the Brownian motion. *Physical Review* **1930**, *36*, DOI: 10.1103/PhysRev.36.823.

(42) Cho, E. C.; Zhang, Q.; Xia, Y. The effect of sedimentation and diffusion on cellular uptake of gold nanoparticles. *Nature Nanotechnology* **2011**, *6*, DOI: 10.1038/nnano.2011.58.

(43) Barbosa, S.; Agrawal, A.; Rodríguez-Lorenzo, L.; Pastoriza-Santos, I.; Alvarez-Puebla, R. A.; Kornowski, A.; Weller, H.; Liz-Marzán, L. M. Tuning size and sensing properties in colloidal gold nanostars. *Langmuir* **2010**, *26*, DOI: 10.1021/la102559e.

(44) Gill, R.; Tian, L.; Somerville, W. R.; Le Ru, E. C.; Van Amerongen, H.; Subramaniam, V. Silver nanoparticle aggregates as highly efficient plasmonic antennas for fluorescence enhancement. *Journal of Physical Chemistry C* **2012**, *116*, DOI: 10.1021/jp305720q.

(45) Stranik, O.; McEvoy, H. M.; McDonagh, C.; MacCraith, B. D. Plasmonic enhancement of fluorescence for sensor applications. Sensors and Actuators, B: Chemical. 2005; DOI: 10.1016/j.snb.2004.08.032.

(46) Emerson, N. T.; Yang, H. Reproducibly Measuring Plasmon-Enhanced Fluorescence in Bulk Solution across a 20-Fold Range of Optical Densities. *Analytical Chemistry* **2021**, *93*, DOI: 10.1021/acs.analchem.1c01210.

(47) Anger, P.; Bharadwaj, P.; Novotny, L. Enhancement and quenching of single-molecule fluorescence. *Physical Review Letters* **2006**, *96*, DOI: 10.1103/PhysRevLett.96.113002.

(48) Rosano, C.; Arosio, P.; Bolognesi, M. The X-ray three-dimensional

structure of avidin. *Biomolecular Engineering* **1999**, *16*, DOI: 10.1016/S1050-3862(99)00047-9.

(49) Kuzuya, A.; Numajiri, K.; Kimura, M.; Komiyama, M. Single-molecule accommodation of streptavidin in nanometer-scale wells formed in DNA nanostructures. *Nucleic acids symposium series (2004)* **2008**, DOI: 10.1093/nass/nrn344.

(50) Jachimska, B.; Pajor, A. Physico-chemical characterization of bovine serum albumin in solution and as deposited on surfaces. *Bioelectrochemistry* **2012**, *87*, DOI: 10.1016/j.bioelechem.2011.09.004.

(51) Weiskirchen, S.; Schröder, S. K.; Buhl, E. M.; Weiskirchen, R. A Beginner's Guide to Cell Culture: Practical Advice for Preventing Needless Problems. *Cells* **2023**, *12*, DOI: 10.3390/cells12050682.

(52) Singh, P.; Carraher, C.; Schwarzbauer, J. E. Assembly of fibronectin extracellular matrix. *Annual Review of Cell and Developmental Biology* **2010**, *26*, DOI: 10.1146/annurev-cellbio-100109-104020.

(53) Shurer, C. R. et al. Physical Principles of Membrane Shape Regulation by the Glycocalyx. *Cell* **2019**, *177*, DOI: 10.1016/j.cell.2019.04.017.

(54) Möckl, L.; Pedram, K.; Roy, A. R.; Krishnan, V.; Gustavsson, A. K.; Dorigo, O.; Bertozzi, C. R.; Moerner, W. E. Quantitative Super-Resolution Microscopy of the Mammalian Glycocalyx. *Developmental Cell* **2019**, *50*, DOI: 10.1016/j.devcel.2019.04.035.

(55) Möckl, L. The Emerging Role of the Mammalian Glycocalyx in Functional Membrane Organization and Immune System Regulation. *Frontiers in Cell and Developmental Biology* **2020**, *8*, DOI: 10.3389/fcell.2020.00253.

(56) Saint Clair, E. C.; Ogren, J. I.; Mamaev, S.; Russano, D.; Kralj, J. M.; Rothschild, K. J. Near-IR resonance Raman spectroscopy of archaerhodopsin 3: Effects

of transmembrane potential. *Journal of Physical Chemistry B* **2012**, *116*, DOI: 10.1021/jp309996a.

(57) Maclaurin, D.; Venkatachalam, V.; Lee, H.; Cohen, A. E. Mechanism of voltage-sensitive fluorescence in a microbial rhodopsin. *Proceedings of the National Academy of Sciences of the United States of America* **2013**, *110*, DOI: 10.1073/pnas.1215595110.

(58) Mei, G.; Mamaeva, N.; Ganapathy, S.; Wang, P.; DeGrip, W. J.; Rothschild, K. J. Analog Retinal Redshifts Visible Absorption of QuasAr Transmembrane Voltage Sensors into Near-infrared. *Photochemistry and Photobiology* **2020**, *96*, DOI: 10.1111/php.13169.

(59) Kandori, H. Biophysics of rhodopsins and optogenetics. 2020.

(60) Kojima, K.; Kurihara, R.; Sakamoto, M.; Takanashi, T.; Kuramochi, H.; Zhang, X. M.; Bito, H.; Tahara, T.; Sudo, Y. Comparative Studies of the Fluorescence Properties of Microbial Rhodopsins: Spontaneous Emission Versus Photointermediate Fluorescence. *Journal of Physical Chemistry B* **2020**, *124*, DOI: 10.1021/acs.jpcb.0c06560.

(61) Wüstner, D.; Christensen, T.; Solanko, L. M.; Sage, D. Photobleaching kinetics and time-integrated emission of fluorescent probes in cellular membranes. *Molecules* **2014**, *19*, DOI: 10.3390/molecules190811096.

(62) Brinks, D.; Castro-Lopez, M.; Hildner, R.; Van Hulst, N. F. Plasmonic antennas as design elements for coherent ultrafast nanophotonics. *Proceedings of the National Academy of Sciences of the United States of America* **2013**, *110*, DOI: 10.1073/pnas.1308652110.

(63) Strohmeyer, N.; Bharadwaj, M.; Costell, M.; Fässler, R.; Müller, D. J. Fibronectin-bound $\alpha5\beta1$ integrins sense load and signal to reinforce adhesion in less than a second. *Nature Materials* **2017**, *16*, DOI: 10.1038/nmat5023.

(64) GitHub repository. https://github.com/Brinkslab/plasmon_gevi.

(65) Guerrero-Martínez, A.; Barbosa, S.; Pastoriza-Santos, I.; Liz-Marzán, L. M. Nanostars shine bright for you. Colloidal synthesis, properties and applications of branched metallic nanoparticles. *Current Opinion in Colloid and Interface Science* **2011**, *16*, DOI: 10.1016/j.cocis.2010.12.007.

(66) Meng, X.; Huismans, L.; Huijben, T.; Szabo, G.; Van Tol, R.; De Heer, I.; Ganapathy, S.; Brinks, D. A compact microscope for voltage imaging. *Journal of Optics (United Kingdom)* **2022**, *24*, DOI: 10.1088/2040-8986/ac5dd5.

(67) Shi, Z.; Graber, Z. T.; Baumgart, T.; Stone, H. A.; Cohen, A. E. Cell Membranes Resist Flow. *Cell* **2018**, *175*, DOI: 10.1016/j.cell.2018.09.054.

(68) Han, X.; Chow, B. Y.; Zhou, H.; Klapoetke, N. C.; Chuong, A.; Rajimehr, R.; Yang, A.; Baratta, M. V.; Winkle, J.; Desimone, R.; Boyden, E. S. A high-light sensitivity optical neural silencer: Development and application to optogenetic control of non-human primate cortex. *Frontiers in Systems Neuroscience* **2011**, DOI: 10.3389/fnsys.2011.00018.

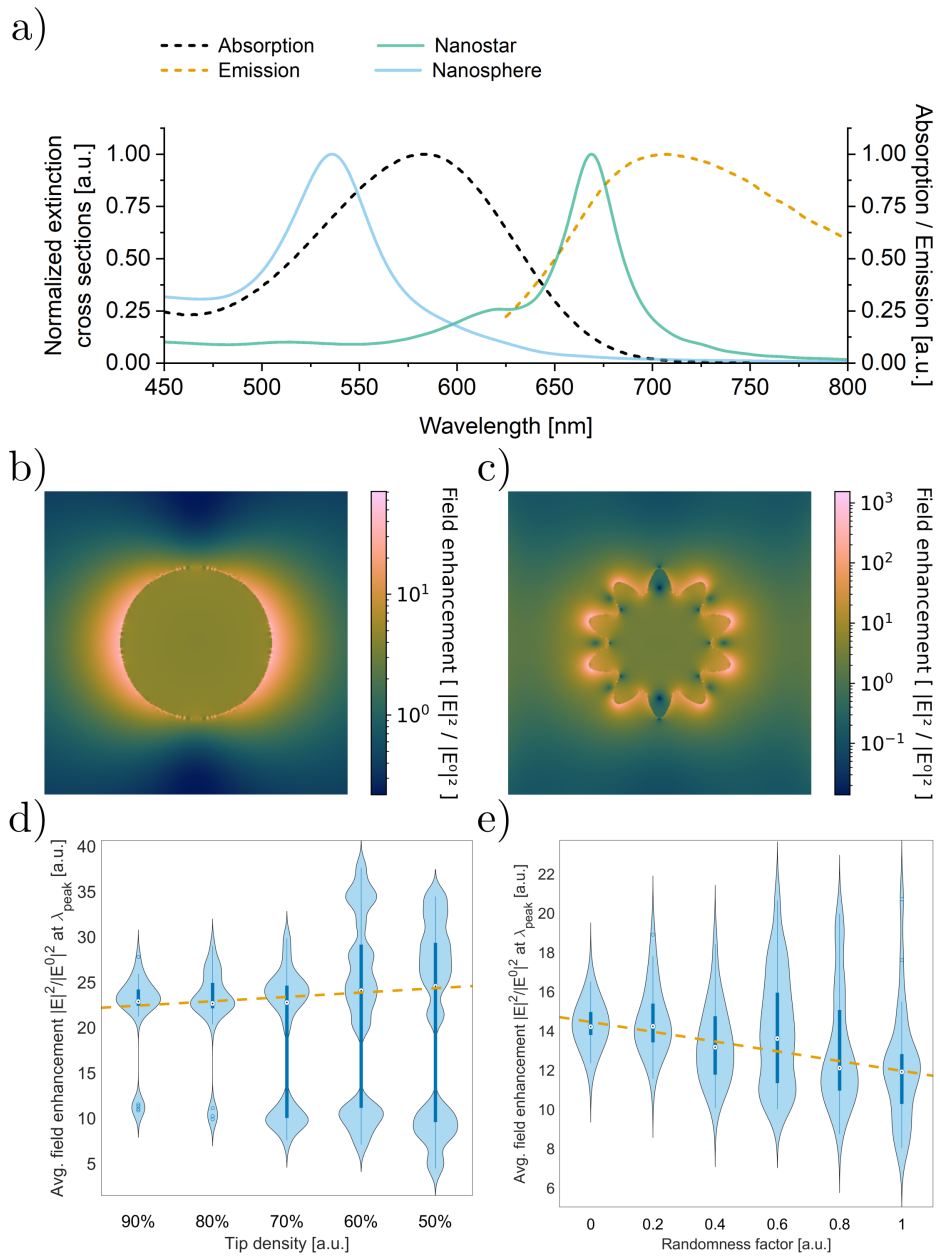

Figure 1: Gold nanostars are optimal candidates for enhancing QuasArs in their disorderly physiological environment, even in the presence of structural irregularities. a, Comparison between the spectra of Archon1 [17] and the FDTD simulated extinction cross sections of respectively a gold nanosphere and a gold nanostar in a watery environment. The simulated nanosphere has a radius of $25nm$. The simulated nanostar has a core radius of $25nm$ and a tip length of $10nm$. The plasmonic resonance of the gold nanostar is close to the peak of the emission spectrum and is thus suitable for plasmonic enhancement. **b,** FDTD simulation of the field enhancement around a gold nanosphere in water at $\lambda = 540nm$. **c,** FDTD simulation of the field enhancement around a gold nanostar in water at $\lambda = 650nm$. The field is confined to a few nanometers around the nanostar spikes. **d,** FDTD simulations of gold nanostars with a core radius of $30nm$ and a tip length of $10nm$, with different tip densities. For each simulation, the positions of the missing tips and the orientation of the nanostar were randomized. The individual results are shown in the Supplementary Information (**Fig. S6**). **e,** FDTD simulations of randomized gold nanostars from an initial ideal particle with a core radius of $30nm$ and a tip length of $10nm$. The tip vertex position and nanostar orientation were randomized for each simulation. The individual results can be found in the Supplementary Information (**Fig. S7**).

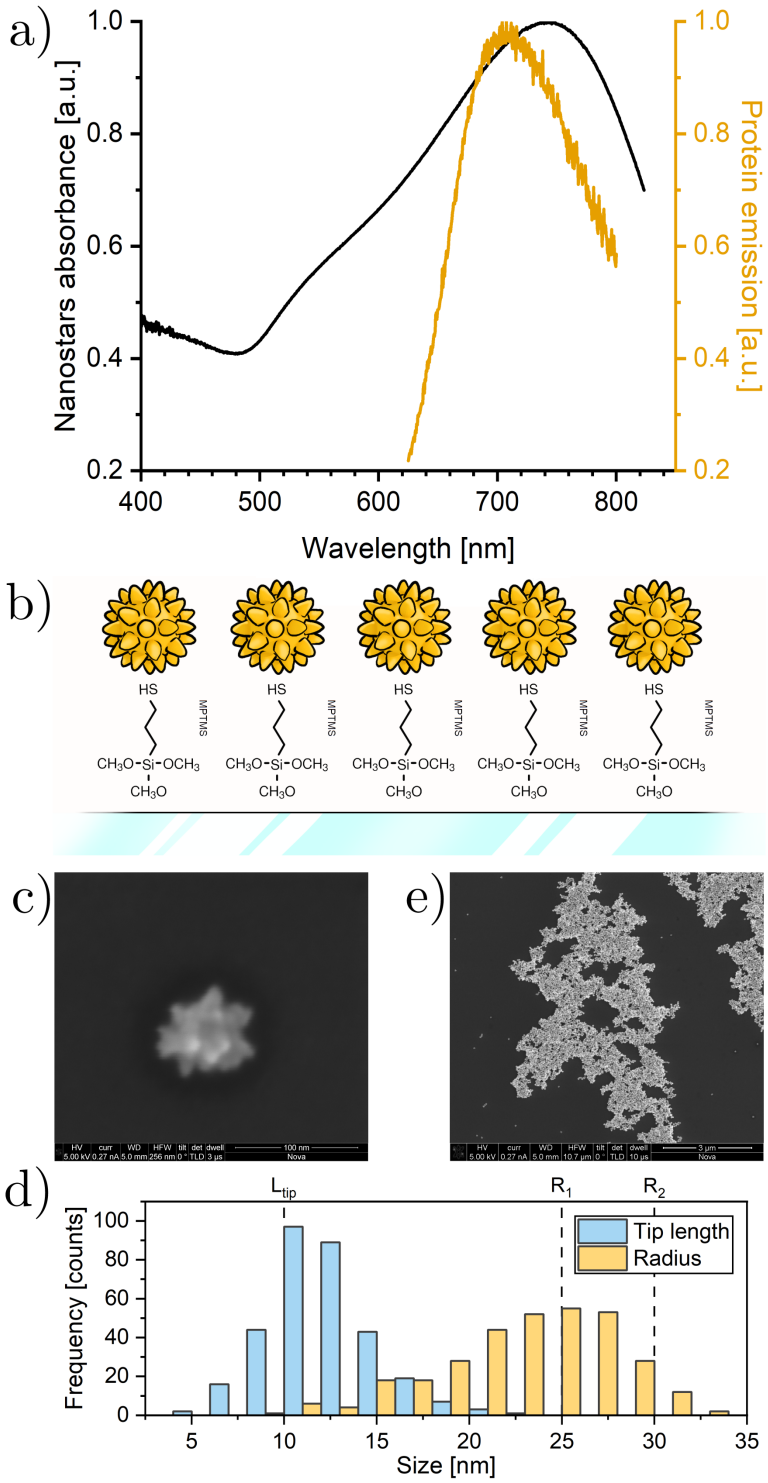

Figure 2: Colloidal gold nanostars are designed to enhance the fluorescence of QuasArs. a, Spectral alignment between the normalized absorbance of the gold nanostars colloid and the fluorescence emission of Archon1.[17] **b,** Illustration of the gold nanostars bound to glass via MPTMS. Not in scale. **c,** SEM micrograph of an isolated gold nanostar. **d,** The physical features of the nanoparticles in SEM images match the ones used for the simulations in **Fig. 1**. **e,** SEM micrograph of a large, complex cluster of gold nanostars.

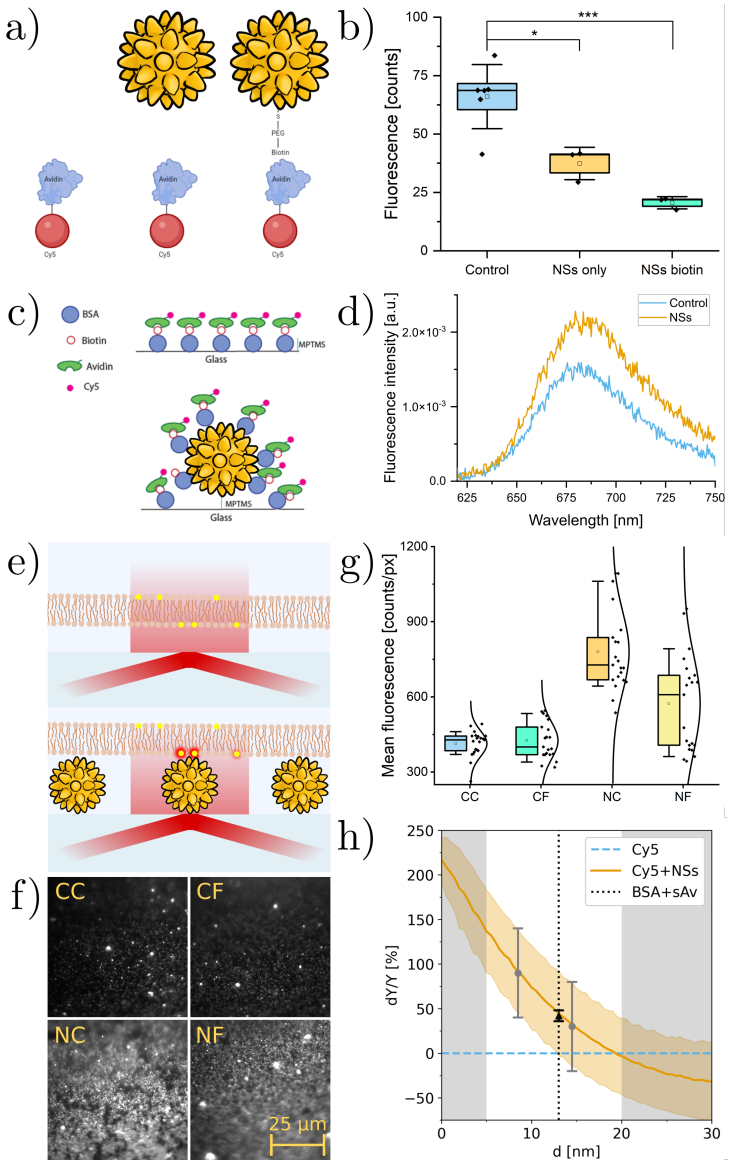

Figure 3: Distance control in nanostar-fluorophore coupling is crucial to enhance the fluorescence emission. a, Illustration of fluorescence assays in solution, employing Cy5 labelled with streptavidin, citrate-capped commercial nanostars and biotin PEGylated gold nanostars. Biotin and streptavidin bind, ensuring a fixed distance between the nanostar and the fluorophore. Not in scale. **b,** Results from fluorescence spectroscopy at peak wavelength. Boxes represent the standard errors, whiskers the SD, squares the means and mid-lines the medians. **c,** Illustration of fluorescence assays on glass substrates. **d,** Results from fluorescence spectroscopy in glass dishes. **e,** Illustrations of TIRF microscopy on a fluorescently-labelled artificial membrane without (top) and with nanostars (bottom). Not in scale. **f,** Median TIRF images of the DOPC/Cy5 artificial membranes. Represented with the same brightness and contrast. **g,** Cross comparison of the fluorescence in DOPC lipid bilayers labelled with Cy5 dye, without or with nanostars (C/N), without or with fibronectin (C/F). Boxes represent the 25-75% range, whiskers the 10-90% range, squares the means and mid-lines the medians. **h,** Predicted mean enhancement of Cy5 (orange, solid line) within the range of uncertainty (orange band, propagated from SD) compared to the natural Y of Cy5 (light blue, dashed line). Data points represent the measured enhancement in panel d (mean as the black triangle, error bar propagated from noise SD) and in panel g (means as the gray dots, error bars propagated from SD). Distances are determined by using the curve as a plasmonic ruler.

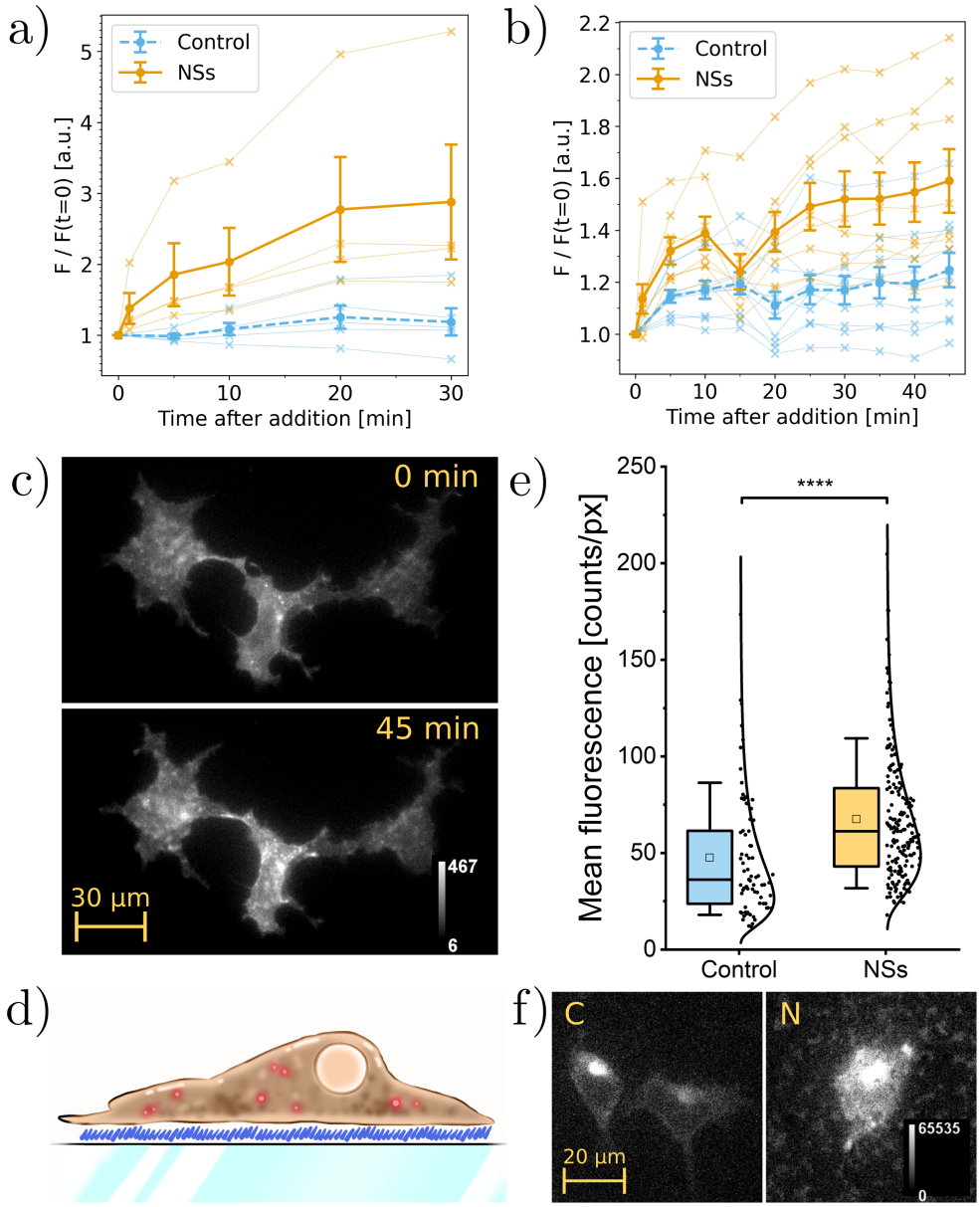

Figure 4: Gold nanostars enable the plasmonic enhancement of QuasArs, in particular QuasAr6a, in living cells. a, Mean fluorescence of cells expressing QuasAr1, normalized to the first frame, after the addition 400μl of nanostars solution (NSs), compared to no addition (control). Error bars correspond to the standard error. Over time, the nanostars gradually diffuse and sediment on the cells, enhancing the fluorescence. **b,** Mean fluorescence of cells expressing QuasAr6a, normalized to the first frame, after the addition 400μl of nanostars solution (NSs), compared to no addition (control). Error bars correspond to the standard error. **c,** Example of fluorescent cells in the QuasAr6a test sample before and after the addition of nanostars. **d,** Illustration of a fluorescent HEK293T cell plated on fibronectin, layered above a glass dish covered in nanostars (in blue). **e,** Screening results show a statistical difference between a sample without (control) and with nanostars (NSs). Boxes represent the 25-75% range, whiskers the 10-90% range, squares the means and mid-lines the medians. Uncertainty propagated from the standard error. **f,** Comparison of the median cell in the control screening (left) and in the nanostars sample (right). Nanostars aggregates are visible either as dim autofluorescence outside the cell, or spot-like shadows under the cell.

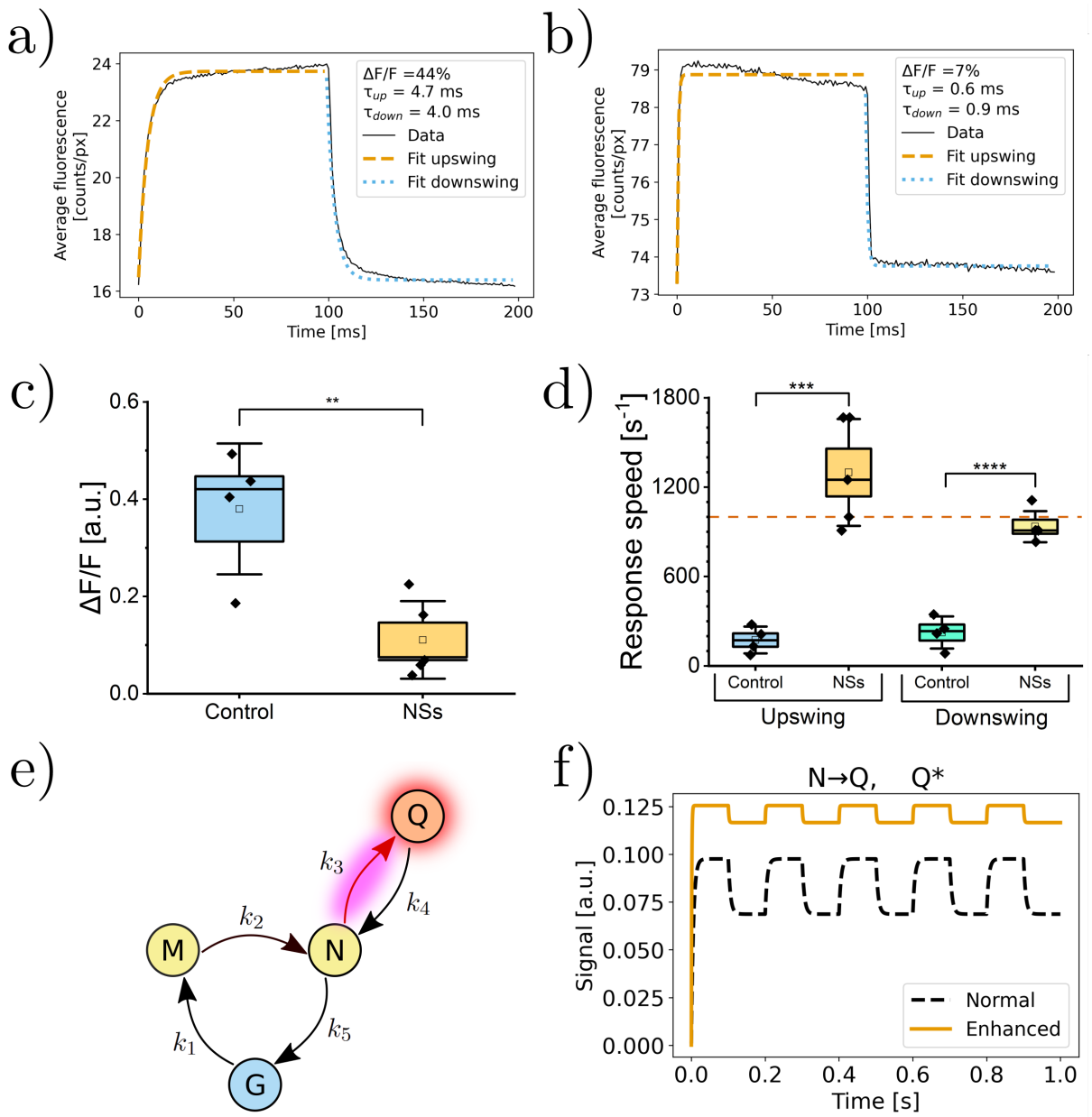

Figure 5: Plasmonic enhancement by gold nanostars manipulates the photocycle of QuasAr6a and causes enhanced brightness, diminished voltage sensitivity and faster kinetics. a, Average trace of the median control cell under the influence of a square wave in membrane potential (−70 mV to +30 mV). **b,** Like a, but in the presence of nanostars. **c,** Voltage sensitivity of QuasAr6a without (control) and with nanostars (NSs). Boxes represent the standard errors, whiskers the standard deviation, squares the means and mid-lines the medians. The mean sensitivity of the control is compatible with the value reported in the literature 0.43 ± 0.04.[24] The mean sensitivity decreases by 71% compared to the control. **d,** Response speed of QuasAr6a without (control) and with nanostars (NSs). Boxes represent the standard errors, whiskers the standard deviation, squares the means and mid-lines the medians. Both the upswing and the downswing transition become faster when the fluorophores are coupled with the nanostars. **e,** Proposed photocycle for QuasAr6a; fluorescence is thought to come from the Q-state, k_2 is voltage-dependent and k_3 is photoactivated. **f,** Numerically simulated traces for the apparent occupancy of the Q-state of QuasAr6a under the influence of a square wave in membrane potential (−70 mV to +30 mV). Plasmonic enhancement is assumed to enhance k_3 and the quantum yield of the Q-state.